

Longitudinal Structure of Quark-Gluon Plasma Unveiled Through Nuclear Deformations

Chunjian Zhang,^{1,2,3} Shengli Huang,¹ and Jiangyong Jia^{1,4}

¹*Department of Chemistry, Stony Brook University, Stony Brook, NY 11794, USA*

²*Shanghai Research Center for Theoretical Nuclear Physics, NSFC and Fudan University, Shanghai 200438, China*

³*Key Laboratory of Nuclear Physics and Ion-beam Application (MOE),*

and Institute of Modern Physics, Fudan University, Shanghai 200433, China

⁴*Physics Department, Brookhaven National Laboratory, Upton, NY 11976, USA**

The study of quark-gluon plasma (QGP) is hindered by our limited understanding of its initial conditions, particularly its longitudinal structure. We propose a novel approach that entails analyzing collisions involving nuclei of similar masses but different deformations. This strategy allows us to vary the initial conditions and collective expansion of the QGP, while minimizing the influence of non-flow correlations. Using a dynamical transport model, we have for the first time extracted the complete longitudinal structure of elliptic flow (v_2). Our findings reveal that although deformation significantly enhances the overall magnitude of v_2 , it does not alter its longitudinal profile. This approach not only enables the separation of the rapidity dependence of flow from its rapidity decorrelations but also prompts further investigation into other nuclear structural features, such as nuclear skin thickness, to advance our understanding of the QGP's initial conditions.

PACS numbers: 25.75.Gz, 25.75.Ld, 25.75.-1

Introduction. High-energy collisions of atomic nuclei at RHIC and the LHC create a hot and dense QGP, whose space-time expansion is well described by the relativistic viscous hydrodynamic equations. Owing to quantum fluctuations in nuclear wavefunctions and the stochastic nature of energy deposition, the initial conditions and subsequent transverse expansion of the QGP vary significantly from one event to another. These variations lead to a range of phenomena accessible in experiments, offering insights into the dynamics and properties of the QGP [1, 2]. Yet, our understanding of the QGP is currently hindered by our limited knowledge of its initial condition. Bridging this gap stands as a pressing challenge in high-energy nuclear physics [3, 4].

The fluctuations in the initial state extend beyond the transverse (xy) plane and are also evident along the longitudinal direction. In a typical picture for nuclear collisions, the energy carried by colliding nucleons are deposited in QCD strings, with significant fluctuations in their starting positions and lengths along pseudorapidity η . Consequently, the shape and size of the initial QGP and its collective flow fluctuate and decorrelate with η even within a single event [5–10]. This picture is supported by measurements of forward-backward fluctuations of multiplicity and anisotropic flow [11–15]. Quantitative assessments of the longitudinal fluctuations (or longitudinal decorrelations), however, are impeded by the limited detector coverage in η and contaminations from non-flow correlations such as jet fragmentation and resonance decays [16]. Moreover, the method to disentangle the average variation of observables as a function of η from decorrelation effects remains experimentally elusive.

In this paper, we propose a new approach to measure longitudinal decorrelations by comparing collisions

of atomic nuclei with similar mass numbers but vastly different shapes. This data-driven approach completely eliminates the influence of non-flow and other short-range correlations. We unveil the complete longitudinal structure of elliptic flow and discuss its implications for the initial condition and expansion dynamics of the QGP.

Method. We demonstrate the idea using elliptic flow $V_2 = v_2 e^{2i\Psi}$, representing the anisotropic distribution of particles in the xy -plane: $dN/d\phi \propto 1 + 2v_2 \cos[2(\phi - \Psi)]$. V_2 captures the hydrodynamic response to the elliptically-shaped overlap region, defined by the eccentricity vector $\mathcal{E}_2 = \varepsilon_2 e^{2i\Phi}$. Both \mathcal{E}_2 and V_2 fluctuate along η within a single collision event [6, 7]. Experimentally, elliptic flow is accessed using the two-particle correlation (2PC) method, which quantifies the second moment of its event-by-event distribution, $v_2\{2\}^2 = V_{2\Delta}(\eta_1, \eta_2) = \langle V_2(\eta_1)V_2^*(\eta_2) \rangle$. The decorrelations manifests as deviations of a factorization ratio from unity:

$$R(\eta_1, \eta_2) = \frac{\langle V_2(\eta_1)V_2^*(\eta_2) \rangle}{\sqrt{\langle V_2(\eta_1)V_2^*(\eta_1) \rangle \langle V_2(\eta_2)V_2^*(\eta_2) \rangle}} < 1 \quad (1)$$

The presence of non-flow correlations concentrated at small relative rapidity $|\Delta\eta| \lesssim 1 - 2$ ($\Delta\eta = \eta_1 - \eta_2$), however, impedes a direct measurement of R . Historically, flow decorrelations were investigated indirectly by correlating reference particles at forward rapidity e.g. $\eta_{\text{ref}} > 4$, with particles of interest at mid-rapidity e.g. $0 < \eta < 2$, using the correlator [11]:

$$r_2(\eta)_{\eta_{\text{ref}}} = \frac{\langle V_2(-\eta)V_2^*(\eta_{\text{ref}}) \rangle}{\langle V_2(\eta)V_2^*(\eta_{\text{ref}}) \rangle} \equiv \frac{R(-\eta, \eta_{\text{ref}})}{R(\eta, \eta_{\text{ref}})}. \quad (2)$$

The second part of the equation is valid for symmetric systems. It is evident that r_2 only captures a limited information of R . Moreover, an *assumption* of r_2 's in-

dependence on η_{ref} is often made to interpret r_2 as a measure of decorrelation between η and $-\eta$.

The shape of the colliding nuclei also impacts the elliptic flow [17–21] and its longitudinal structure [22]. Most nuclei are non-spherical, exhibiting either prolate or oblate shapes characterized by the quadrupole deformation parameter β . The event-wise initial state eccentricity vector comprises a component corresponding to the spherical nuclei and another arising from deformation: $\mathcal{E}_2 = \mathcal{E}_{2,\text{sp}} + \mathcal{E}_{2,\beta}$. The $\mathcal{E}_{2,\beta} \approx p(\Omega_1, \Omega_2)\beta$ depends on the Euler angle Ω of the two colliding nuclei and is uncorrelated with $\mathcal{E}_{2,\text{sp}}$, e.g. $\langle \mathcal{E}_{2,\text{sp}} \mathcal{E}_{2,\beta}^* \rangle = 0$ [23]. Consequently, the elliptic flow in each collision event is the sum of two uncorrelated components: $V_2 = V_{2,\text{sp}} + V_{2,\beta}$. The flow measured via the 2PC method contains independent contributions from these sources along with non-flow δ_{nf} that primarily depends on $\Delta\eta$:

$$\begin{aligned} V_{2\Delta} &= V_{2\Delta,\text{sp}} + V_{2\Delta,\beta} + \delta_{\text{nf}} \\ &= a(\eta_1, \eta_2) + b(\eta_1, \eta_2)\beta^2 + \delta_{\text{nf}}(|\eta_1 - \eta_2|) \end{aligned} \quad (3)$$

Both spherical baseline a and deformation component $b\beta^2$ may exhibit rapidity dependencies. In ultra-central collisions, the $\mathcal{E}_{2,\text{sp}}$, and thus $V_{2\Delta,\text{sp}}$, are driven by nucleon random fluctuations, and are inversely proportional to the mass number A , $V_{2\Delta,\text{sp}} \propto 1/A$ [24].

Ideally, the rapidity structure of the deformation-induced component can be isolated by comparing isobar pairs $X + X$ and $Y + Y$ with different β values:

$$b(\eta_1, \eta_2) = (V_{2\Delta,X+X} - V_{2\Delta,Y+Y}) / (\beta_{X+X}^2 - \beta_{Y+Y}^2) \quad (4)$$

The subtraction of $V_{2\Delta}$ eliminates the spherical baseline and non-flow contributions, facilitating direct explorations of the QGP's longitudinal structure. An available pair for this purpose is $^{238}\text{U} + ^{238}\text{U}$ and $^{197}\text{Au} + ^{197}\text{Au}$ collisions, acquired by the STAR experiment at RHIC. U has large prolate deformation, while Au is mildly oblate. We focus on the most central collisions, where the impact of the deformation is most significant.

Setup. Our analysis is performed using the transport model, AMPT [25], which simulates the full 3D evolution of heavy-ion collisions event by event. The distribution of nucleons in nuclei is sampled from a Woods-Saxon parameterization in polar coordinate: $\rho(r, \theta) \propto [1 + \exp((r - R_0(1 + \beta Y_{2,0}(\theta))/a_0))]^{-1}$. Collisions for three configurations are simulated, each characterized by distinct geometrical parameters as listed in Table I. The collision events are generated at $\sqrt{s_{\text{NN}}} = 193$ GeV for U+U and $\sqrt{s_{\text{NN}}} = 200$ GeV for Au+Au, employing the string-melting mode with a partonic cross-section of 3 mb. We calculate eccentricity for forward-going, backward-going and all participating nucleons, denoted as $\mathcal{E}_{2,\text{F}}$, $\mathcal{E}_{2,\text{B}}$ and \mathcal{E}_2 , respectively. The particles for the 2PC analysis are chosen from the transverse momentum range $0.2 < p_{\text{T}} < 3$ GeV/c and pseudorapidity range $|\eta| < 5$. Event central-

ity is defined by charged particle multiplicity in $|\eta| < 0.5$ (N_{ch}).

System	$^{238}\text{U} + ^{238}\text{U}$	$^{238}\text{U} + ^{238}\text{U}$	$^{197}\text{Au} + ^{197}\text{Au}$
$\beta, R_0(\text{fm}), a_0(\text{fm})$	0.28, 6.81, 0.55	0, 6.81, 0.55	-0.14, 6.62, 0.52

TABLE I. Nuclei species and their quadrupole deformation β , radius R_0 and skin thickness a_0 used in AMPT simulation.

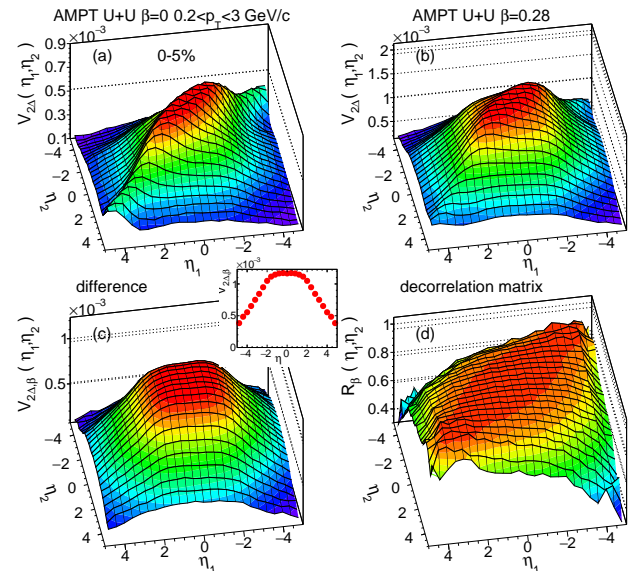


FIG. 1. The elliptic flow from 2PC method, $V_{2\Delta}(\eta_1, \eta_2)$, in 0–5% most central U+U collisions with deformation $\beta = 0.28$ (a), no deformation $\beta = 0$ (b), and their difference $V_{2\Delta,\beta} = V_{2\Delta}\{\beta = 0.28\} - V_{2\Delta}\{\beta = 0\}$ (c). The $V_{2\Delta,\beta}$ is separated into the η dependence of elliptic flow, $[v_2\{2\}(\eta)]^2 \equiv V_{2\Delta,\beta}(\eta, \eta)$, in the inset of panel (c) and the flow decorrelations in panel (d), captured by the factorization ratio $R_\beta(\eta_1, \eta_2)$.

Result. Figure 1(a) shows the two-dimensional distribution of $V_{2\Delta}(\eta_1, \eta_2)$ in 0–5% central U+U collisions without deformation. A notable diagonal ridge along $\eta_+ = (\eta_1 + \eta_2)/2$ within $|\Delta\eta| < 2$ is observed, indicating contributions from non-flow and/or other short-range correlations driven by localized hot spots in the initial state [26]. Beneath this diagonal ridge lies a broader distribution whose amplitude decreases with η_+ and $\Delta\eta$, reflecting a decrease of flow with η and the effects of flow decorrelations, respectively. Deformation enhances $V_{2\Delta}$ by about a factor of two (Fig. 1(b)), and this enhancement (Fig. 1(c)) represents the deformation-induced component $V_{2\Delta,\beta} = b\beta^2$. We found that the shape of $V_{2\Delta,\beta}$ is indeed independent of the β value used.

The $V_{2\Delta,\beta}$ exhibits a broad shape in pseudorapidity. Its values along the diagonal direction, $V_{2\Delta,\beta}(\eta, \eta) = \langle V_{2,\beta}(\eta)V_{2,\beta}^*(\eta) \rangle$ (inset), capture the η dependence of flow without any decorrelation effects. This flow signal remains nearly constant for $|\eta| < 2$ but then decreases at larger η . To isolate decorrelations of flow from its η

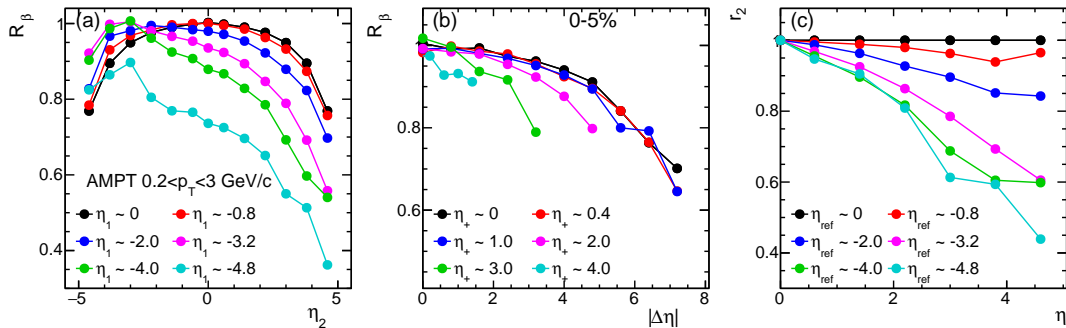


FIG. 2. Projections of R_β in bottom-right panel of Fig. 1 along the vertical direction as a function of η_2 (a) and diagonal direction as a function of $\Delta\eta$ (b), as well as the $r_2 = R_\beta(-\eta, \eta_{\text{ref}})/R_\beta(\eta, \eta_{\text{ref}})$ calculated using different η_{ref} (c).

dependence, we compute the 2D matrix in Eq. (1) and display the resulting $R(\eta_1, \eta_2)$ in Fig. 1(d).

To dissect the trends in Fig. 1(d), we depict the values of R in narrow slices along the vertical or diagonal directions in Fig. 2(a) and Fig. 2(b), respectively. Vertical slices capture the decorrelation of particles at η_2 relative to the reference particles at η_1 . Notably, for reference particles at far-backward rapidity $\eta_1 \sim -5$, the decorrelations are stronger towards positive η_2 . Conversely, when reference particles are situated at midrapidity $\eta_1 \sim 0$, the decorrelations are negligible up to $\eta_2 \sim 2$ before turning on quickly. These trends manifest differently in the diagonal slices in Fig. 2(b), which displays decorrelation as a function of η_+ for pairs at a fixed $\Delta\eta$. Evidently, pairs at a given $\Delta\eta$ generally exhibit less decorrelation around mid-rapidity than those at larger rapidity.

Figure 2(c) displays the r_2 calculated via Eq. (2). Since non-flow is absent in $R(\eta_1, \eta_2)$, r_2 can be calculated for any η_{ref} . Remarkably, the values of r_2 depend on the choice of η_{ref} , in particular for $\eta_{\text{ref}} \lesssim 3$. This result indicates that the common notion [11, 13, 27] that r_2 measures the decorrelation between η and $-\eta$ is incorrect.

Having investigated decorrelations of the deformation-induced component, we next explore the decorrelations of the normal component $V_{2\Delta, \text{sp}}(\eta_1, \eta_2)$. As demonstrated below, there are strong evidences that decorrelations of long-range part of $V_{2\Delta, \text{sp}}$ is quite similar to that of $V_{2\Delta, \beta}$.

Let's first emphasize the well-established fact that the decorrelation of V_2 is driven by the difference between $\mathcal{E}_{2, \text{F}}$ and $\mathcal{E}_{2, \text{B}}$. This interpretation arises because the initial-state geometry at forward (backward) rapidity aligns more with $\mathcal{E}_{2, \text{F}}$ ($\mathcal{E}_{2, \text{B}}$), while at mid-rapidity, it is driven by $\mathcal{E}_2 \sim (\mathcal{E}_{2, \text{F}} + \mathcal{E}_{2, \text{B}})/2$ [6, 27]. Hence, V_2 decorrelation can be approximated by its projection along $\mathcal{E}_{2, \text{B}}$,

$$v_{2, \varepsilon \text{B}}(\eta) \equiv \frac{\langle V_2(\eta) \mathcal{E}_{2, \text{B}}^* \rangle}{\sqrt{\langle \mathcal{E}_{2, \text{B}} \mathcal{E}_{2, \text{B}}^* \rangle}} \quad (5)$$

Figure 3(a) shows the results in 0–5% centrality with (without) deformation, $v_{2, \varepsilon \text{B}}(\eta)$ ($v_{2, \varepsilon \text{B}, \text{sp}}(\eta)$), along with

the deformation-induced component calculated as

$$v_{2, \varepsilon \text{B}, \beta}(\eta) \equiv \frac{\langle V_2(\eta) \mathcal{E}_{2, \text{B}, \beta}^* \rangle}{\sqrt{\langle \mathcal{E}_{2, \text{B}, \beta} \mathcal{E}_{2, \text{B}, \beta}^* \rangle}} = \frac{\langle V_2(\eta) \mathcal{E}_{2, \text{B}}^* \rangle_{\beta=0.28} - \langle V_2(\eta) \mathcal{E}_{2, \text{B}}^* \rangle_{\beta=0}}{\sqrt{\langle \mathcal{E}_{2, \text{B}} \mathcal{E}_{2, \text{B}}^* \rangle_{\beta=0.28} - \langle \mathcal{E}_{2, \text{B}} \mathcal{E}_{2, \text{B}}^* \rangle_{\beta=0}}}, \quad (6)$$

satisfying the relation $[v_{2, \varepsilon \text{B}, \beta}(\beta=0.28)]^2 = v_{2, \varepsilon \text{B}, \text{sp}}^2 + v_{2, \varepsilon \text{B}, \beta}^2$. Large asymmetries in η are observed for all cases. We further overlay the 2PC flow from Fig. 1(c) for $\eta_{\text{ref}} = 4-5$:

$$v_{2, \eta_{\text{ref}}, \beta}(\eta) = \frac{V_{2\Delta, \beta}(\eta, \eta_{\text{ref}})}{\sqrt{V_{2\Delta, \beta}(\eta_{\text{ref}}, \eta_{\text{ref}})}} \quad (7)$$

Since reference particles are chosen from very forward rapidity, $v_{2, \eta_{\text{ref}}, \beta}$ should resemble $v_{2, \varepsilon \text{B}, \beta}$. In reality, $v_{2, \varepsilon \text{B}, \beta} \approx 0.75 v_{2, \eta_{\text{ref}}, \beta}$, implying that part of the flow signal is not driven by participant eccentricity (instead by local hot spots [28]).

We quantify eccentricity-induced decorrelations via $r_{2, \varepsilon \text{B}} = v_{2, \varepsilon \text{B}}(\eta)/v_{2, \varepsilon \text{B}}(-\eta)$, defined similar to Eq. (2). The results in 0–5% centrality are displayed in Fig. 3 (b). Significant decreases with η are observed in all four cases: eccentricity-driven flow with and without deformation $v_{2, \varepsilon \text{B}, \beta}$ and $v_{2, \varepsilon \text{B}, \text{sp}}$, and the deformation-induced components $v_{2, \varepsilon \text{B}, \beta}$ and $v_{2, \eta_{\text{ref}}, \beta}$. Remarkably, all cases show nearly identical trends, suggesting flow component corresponding to spherical nuclei and the component driven by deformation have similar longitudinal structure. However, the decorrelation of spherical baseline is slightly larger than deformation-induced component in 0–2% central collisions (see Appendix).

Our analysis hinges on the complete elimination of non-flow and other short-range correlations to unveil the full longitudinal structure of V_2 . Ideally, this can be achieved only through a comparison between systems with the same A , such as U+U with and without deformation. For the comparison between $^{197}\text{Au}+^{197}\text{Au}$ and $^{238}\text{U}+^{238}\text{U}$, the non-flow contributions at the same centrality do not cancel, given a 20% difference in their masses. This can be fixed by introduce a scale factor in the subtraction,

$$V_{2\Delta, \beta}^{\text{U-Au}} = V_{2\Delta, \text{U}}\{\beta=0.28\} - \frac{\langle N_{\text{ch}} \rangle_{\text{Au}}}{\langle N_{\text{ch}} \rangle_{\text{U}}} V_{2\Delta, \text{Au}}\{\beta=-0.14\}. \quad (8)$$

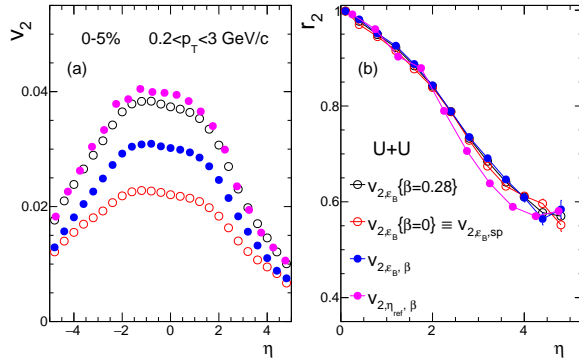


FIG. 3. Left: Comparison of the flow calculated using the initial state eccentricity of backward-going nucleon participants v_{2,ϵ_B} in Eq. (5) in U+U collisions with $\beta = 0.28$ (open-black circles) and $\beta = 0$ (open-red circles), the difference between the two (solid-blue circles). They reflect the magnitudes of V_2 projected along $\mathcal{E}_{2,B}$. The solid-pink circles show the deformation-driven elliptic flow obtained directly from two-particle methods via distributions like those in Fig. 1(c). Right: The ratios of distribution $\mathcal{O}(\eta)$, calculated as $r_2 = \mathcal{O}(\eta)/\mathcal{O}(-\eta)$, for the four distributions in the top panels, reflecting the flow decorrelations measured in the traditional methods. Results are obtained in the 0–5% most central U+U collisions.

Here, $\langle N_{\text{ch}} \rangle$ denotes the average charge particle multiplicity in the chosen centrality range. This works because the 2PC non-flow is expected to scale inversely with N_{ch} in the absence of medium effects: $\delta_{\text{nf}} \propto 1/N_{\text{ch}} \propto 1/A$ [29, 30]. This scaling factor also ensures the cancellation of the spherical baseline since $V_{2\Delta,\text{sp}} \propto 1/A$.

Figure 4(a) presents the $R(\eta_1, \eta_2)$ derived from $V_{2\Delta,\beta}^{\text{U-Au}}$ via Eq. (8). The shape of the distribution resembles Fig. 1(d), indicating that non-flow correlations are effectively eliminated¹. Consequently, the decorrelations inferred from R (Fig. 4(b)) and r_2 (Fig. 4(c)) resembles the ideal cases with non-flow completely eliminated.

Summary. We introduce a novel approach to probe the longitudinal structure of QGP in central high-energy nuclear collisions by comparing two systems involving nuclei with similar mass but differing shapes. By measuring the difference of two-particle azimuthal correlation in $^{238}\text{U}+^{238}\text{U}$ and $^{197}\text{Au}+^{197}\text{Au}$ collisions, we extract the component of the elliptic flow induced by the large quadrupole deformation of ^{238}U : $V_{2\Delta,\beta}(\eta_1, \eta_2)$. This extraction via Eq. (8) effectively subtracts out non-flow correlations, unveiling the decorrelation of $V_{2\Delta,\beta}$ over the full η_1 and η_2 space. Using a transport model simulation, we found that the decorrelations for pairs with a given $\Delta\eta$ is stronger at large rapidity than at mid-

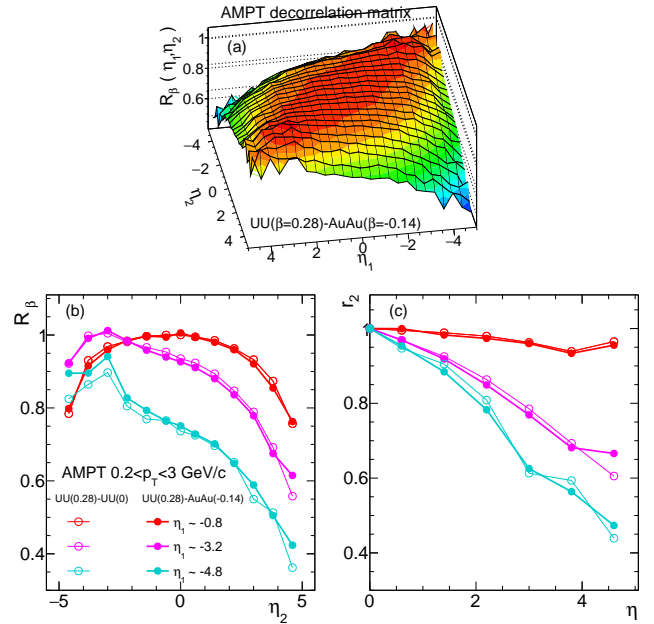


FIG. 4. Top: The factorization ratio R_β for $V_{2\Delta,\beta}^{\text{U-Au}}$ obtained from the difference between U+U and Au+Au collisions via Eq. (8) (similar to Fig. 1(d)). Bottom: Slices of R_β along the vertical direction (b) as well as the r_2 calculated using different η_{ref} (c). They are compared with results obtained by subtracting U+U collisions with deformation from U+U collisions without deformation in Fig. 2.

rapidity. This non-uniform decorrelations results from η -dependent eccentricity that interpolate between $\mathcal{E}_{2,F}$ and $\mathcal{E}_{2,B}$, driven by the forward-going and backward-going nucleons, respectively. Moreover, the decorrelations of deformation-induced flow is found to be similar to decorrelations of its spherical baseline. Our method extends the concept of event-shape engineering [31] but circumvents its inherent selection bias. Therefore, this “event-shape design” data-driven approach could be used to map out the QGP’s longitudinal structure by comparing $^{238}\text{U}+^{238}\text{U}$ and $^{197}\text{Au}+^{197}\text{Au}$ at RHIC, $^{129}\text{Xe}+^{129}\text{Xe}$ and $^{208}\text{Pb}+^{208}\text{Pb}$ at the LHC, or the recently proposed small collision systems $^{16}\text{O}+^{16}\text{O}$ and $^{20}\text{Ne}+^{20}\text{Ne}$ [32].

The idea of probing initial state via nuclear structure knowledge goes beyond nuclear shapes. In fact, other global properties of atomic nuclei, such as the nuclear radius R_0 and nuclear skin a_0 , can be similarly employed to probe the initial conditions. The STAR experiment has collected data on $^{96}\text{Ru}+^{96}\text{Ru}$ and $^{96}\text{Zr}+^{96}\text{Zr}$ collisions, which, in addition to their differing shapes, also possess distinct a_0 and R_0 values. The R_0 and a_0 have been shown to impact several bulk observables in mid-central collisions, including the N_{ch} distribution, v_2 and mean p_T [33–35]. Investigating the rapidity dependence of bulk observables and their differences between Ru+Ru and Zr+Zr collisions could further constrain the longitudi-

¹ Not using the scale factor in Eq. (8) would result in a shallow minimum along the diagonal direction, indicative of over-subtraction of non-flow.

dinal structure of QGP's initial conditions in a broad centrality range. We leave this intriguing prospect for future study.

We thank Somadutta Bhatta and Giuliano Giacalone for useful discussions. This work is supported by DOE Research Grant Number DE-SC0024602.

APPENDIX

Figure 5 displays the longitudinal decorrelations in ultra-central 0–2% collisions, similar to Fig. 3. While the general trends resemble those observed in the 0–5% centrality, the overall strength of decorrelations are stronger, consistent with previous findings regarding the centrality dependence of flow decorrelations [11]. Meanwhile, the $r_2\{v_{2,\varepsilon_B}\}$ without deformation (open-red) shows a somewhat stronger decrease compared to that with deformation (open-black), implying that decorrelations of $V_{2\Delta,sp}$ is also stronger than that of $V_{2\Delta,\beta}$. This subtle difference between the deformation-induced component and its spherical baseline is apparent only in ultra-central collisions, attributable to the tendency of the symmetry axes of the two nuclei to align in these collisions, which we discuss below.

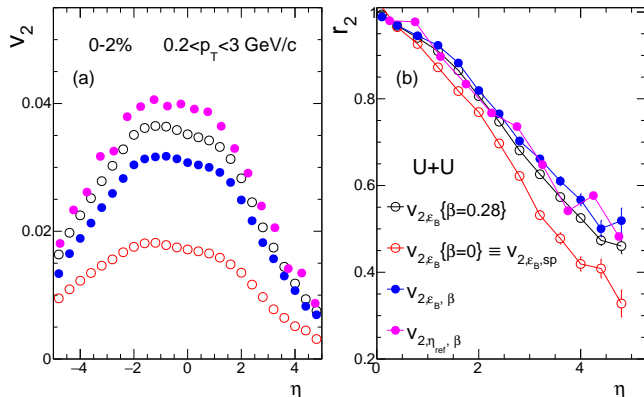


FIG. 5. Left: Comparison of the flow calculated using the initial state eccentricity of backward-going nucleon participants v_{2,ε_B} in Eq. (5) in U+U collisions with $\beta = 0.28$ (open-black circles) and $\beta = 0$ (open-red circles), the difference between the two (solid-blue circles). They reflect the magnitudes of V_2 projected along $\mathcal{E}_{2,B}$. The solid-pink circles show the deformation-driven elliptic flow obtained directly from two-particle methods via distributions like those in Fig. 1(c). Right: The ratios of distribution $\mathcal{O}(\eta)$, calculated as $r_2 = \mathcal{O}(\eta)/\mathcal{O}(-\eta)$, for the four distributions in the top panels, reflecting the flow decorrelations measured in the traditional methods. Results are obtained in the 0–2% most central U+U collisions.

The longitudinal structure of the QGP's initial ellipticity interpolates between $\mathcal{E}_{2,F}$ at the forward rapidity and $\mathcal{E}_{2,B}$ at the backward rapidity. Therefore, the decorrelations in Figs. 3 and 5 are expected to reflect the decorre-

lations between $\mathcal{E}_{2,F}$ and $\mathcal{E}_{2,B}$ characterized by:

$$R_\varepsilon^{F-B} = \frac{\langle \mathcal{E}_{2,F} \mathcal{E}_{2,B}^* \rangle}{\sqrt{\langle \mathcal{E}_{2,F} \mathcal{E}_{2,F}^* \rangle \langle \mathcal{E}_{2,B} \mathcal{E}_{2,B}^* \rangle}}. \quad (9)$$

This quantity captures the origin of the flow decorrelations defined in Eq. (1). The centrality dependence of R_ε^{F-B} is displayed in Fig. 6 for U+U collisions with and without deformation. The presence of deformation increases the values of R_ε^{F-B} in 0–2% centrality range, implying less decorrelations. Beyond the 2% centrality, the deformation has little impact on R_ε^{F-B} . These behaviors naturally explain the ordering of the decorrelation seen in Fig. 5 (b).

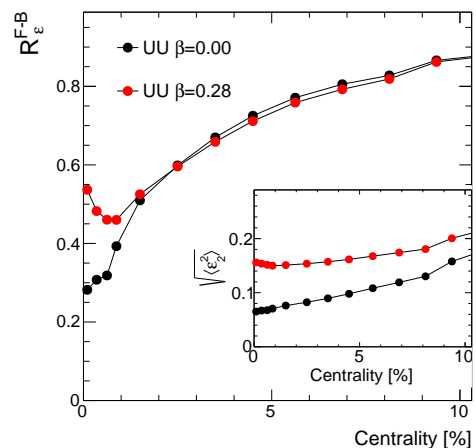


FIG. 6. Centrality dependence of R_ε^{F-B} defined in Eq. (9) for U+U collisions with and without deformation. The inset shows the rms values of the ε_2 for the two cases.

On the other hand, the magnitudes of the eccentricity, in terms of its mean-square values, are consistently enhanced by deformation over a much larger centrality range, as shown in the inset. Evidently, deformation always enhances the value of $\langle \varepsilon_2^2 \rangle$, but may not necessarily lead to a better alignment of the two eccentricity vectors $\mathcal{E}_{2,F}$ and $\mathcal{E}_{2,B}$ ². The alignment of eccentricity vectors in 0–2% centrality is the result of requiring large N_{ch} which prefers an alignment in the orientations of their symmetry axes. Selection of central but not ultra-central collisions does not fully enforce such alignment, and the orientations of the two nuclei hence are partially random with respect to each other.

² Both $\mathcal{E}_{2,F}$ and $\mathcal{E}_{2,B}$ have a deformation component $\mathcal{E}_{2,\beta}$, statistically uncorrelated with each other. In a Glauber model, it is easy to show that the mean square value of total eccentricity $\mathcal{E}_2 = (\mathcal{E}_{2,F} + \mathcal{E}_{2,B})/2$ is enhanced by $\langle \mathcal{E}_{2,\beta} \mathcal{E}_{2,\beta}^* \rangle / 2$. For full alignment, the enhancement would be $\langle \mathcal{E}_{2,\beta} \mathcal{E}_{2,\beta}^* \rangle$.

-
- * Correspond to jiangyong.jia@stonybrook.edu
- [1] P. Romatschke and U. Romatschke, *Relativistic Fluid Dynamics In and Out of Equilibrium*, Cambridge Monographs on Mathematical Physics (Cambridge University Press, 2019) [arXiv:1712.05815](https://arxiv.org/abs/1712.05815) [nucl-th].
- [2] W. Busza, K. Rajagopal, and W. van der Schee, *Ann. Rev. Nucl. Part. Sci.* **68**, 339 (2018), [arXiv:1802.04801](https://arxiv.org/abs/1802.04801) [hep-ph].
- [3] P. Achenbach *et al.*, *Nucl. Phys. A* **1047**, 122874 (2024), [arXiv:2303.02579](https://arxiv.org/abs/2303.02579) [hep-ph].
- [4] B. Bally *et al.*, (2022), [arXiv:2209.11042](https://arxiv.org/abs/2209.11042) [nucl-ex].
- [5] P. Bozek, W. Broniowski, and J. Moreira, *Phys. Rev. C* **83**, 034911 (2011), [arXiv:1011.3354](https://arxiv.org/abs/1011.3354) [nucl-th].
- [6] J. Jia and P. Huo, *Phys. Rev. C* **90**, 034915 (2014), [arXiv:1403.6077](https://arxiv.org/abs/1403.6077) [nucl-th].
- [7] L.-G. Pang, H. Petersen, G.-Y. Qin, V. Roy, and X.-N. Wang, *Eur. Phys. J. A* **52**, 97 (2016), [arXiv:1511.04131](https://arxiv.org/abs/1511.04131) [nucl-th].
- [8] J. Jia, S. Radhakrishnan, and M. Zhou, *Phys. Rev. C* **93**, 044905 (2016), [arXiv:1506.03496](https://arxiv.org/abs/1506.03496) [nucl-th].
- [9] X.-Y. Wu, L.-G. Pang, G.-Y. Qin, and X.-N. Wang, *Phys. Rev. C* **98**, 024913 (2018), [arXiv:1805.03762](https://arxiv.org/abs/1805.03762) [nucl-th].
- [10] C. Shen and B. Schenke, *Phys. Rev. C* **97**, 024907 (2018), [arXiv:1710.00881](https://arxiv.org/abs/1710.00881) [nucl-th].
- [11] V. Khachatryan *et al.* (CMS), *Phys. Rev. C* **92**, 034911 (2015), [arXiv:1503.01692](https://arxiv.org/abs/1503.01692) [nucl-ex].
- [12] M. Aaboud *et al.* (ATLAS), *Eur. Phys. J. C* **78**, 142 (2018), [arXiv:1709.02301](https://arxiv.org/abs/1709.02301) [nucl-ex].
- [13] G. Aad *et al.* (ATLAS), *Phys. Rev. Lett.* **126**, 122301 (2021), [arXiv:2001.04201](https://arxiv.org/abs/2001.04201) [nucl-ex].
- [14] S. Acharya *et al.* (ALICE), *Phys. Lett. B* **781**, 20 (2018), [arXiv:1710.07975](https://arxiv.org/abs/1710.07975) [nucl-ex].
- [15] M. Aaboud *et al.* (ATLAS), *Phys. Rev. C* **95**, 064914 (2017), [arXiv:1606.08170](https://arxiv.org/abs/1606.08170) [hep-ex].
- [16] Z. Xu, X. Wu, C. Sword, G. Wang, S. A. Voloshin, and H. Z. Huang, *Phys. Rev. C* **105**, 024902 (2022), [arXiv:2012.06689](https://arxiv.org/abs/2012.06689) [nucl-ex].
- [17] P. Filip, R. Lednicky, H. Masui, and N. Xu, *Phys. Rev. C* **80**, 054903 (2009).
- [18] Q. Y. Shou, Y. G. Ma, P. Sorensen, A. H. Tang, F. Videbæk, and H. Wang, *Phys. Lett. B* **749**, 215 (2015), [arXiv:1409.8375](https://arxiv.org/abs/1409.8375) [nucl-th].
- [19] L. Adamczyk *et al.* (STAR), *Phys. Rev. Lett.* **115**, 222301 (2015), [arXiv:1505.07812](https://arxiv.org/abs/1505.07812) [nucl-ex].
- [20] STAR Collaboration, (2024), [arXiv:2401.06625](https://arxiv.org/abs/2401.06625) [nucl-ex].
- [21] G. Giacalone, *Eur. Phys. J. A* **59**, 297 (2023), [arXiv:2305.19843](https://arxiv.org/abs/2305.19843) [nucl-th].
- [22] M. Nie, C. Zhang, Z. Chen, L. Yi, and J. Jia, *Phys. Lett. B* **845**, 138177 (2023), [arXiv:2208.05416](https://arxiv.org/abs/2208.05416) [nucl-th].
- [23] J. Jia, *Phys. Rev. C* **105**, 044905 (2022), [arXiv:2109.00604](https://arxiv.org/abs/2109.00604) [nucl-th].
- [24] J.-P. Blaizot, W. Broniowski, and J.-Y. Ollitrault, *Phys. Rev. C* **90**, 034906 (2014), [arXiv:1405.3274](https://arxiv.org/abs/1405.3274) [nucl-th].
- [25] Z.-W. Lin, C. M. Ko, B.-A. Li, B. Zhang, and S. Pal, *Phys. Rev. C* **72**, 064901 (2005), [arXiv:nuc1-th/0411110](https://arxiv.org/abs/nuc1-th/0411110).
- [26] L. Pang, Q. Wang, and X.-N. Wang, *Phys. Rev. C* **89**, 064910 (2014), [arXiv:1309.6735](https://arxiv.org/abs/1309.6735) [nucl-th].
- [27] A. Behera, M. Nie, and J. Jia, *Phys. Rev. Res.* **2**, 023362 (2020), [arXiv:2003.04340](https://arxiv.org/abs/2003.04340) [nucl-th].
- [28] In preparation,.
- [29] S. Chatrchyan *et al.* (CMS), *Phys. Lett. B* **724**, 213 (2013), [arXiv:1305.0609](https://arxiv.org/abs/1305.0609) [nucl-ex].
- [30] M. I. Abdulhamid *et al.* (STAR), *Phys. Rev. Lett.* **130**, 242301 (2023), [arXiv:2210.11352](https://arxiv.org/abs/2210.11352) [nucl-ex].
- [31] J. Schukraft, A. Timmins, and S. A. Voloshin, *Phys. Lett. B* **719**, 394 (2013), [arXiv:1208.4563](https://arxiv.org/abs/1208.4563) [nucl-ex].
- [32] G. Giacalone *et al.*, (2024), [arXiv:2402.05995](https://arxiv.org/abs/2402.05995) [nucl-th].
- [33] J. Jia and C. Zhang, *Phys. Rev. C* **107**, L021901 (2023), [arXiv:2111.15559](https://arxiv.org/abs/2111.15559) [nucl-th].
- [34] J. Jia, G. Giacalone, and C. Zhang, *Phys. Rev. Lett.* **131**, 022301 (2023), [arXiv:2206.10449](https://arxiv.org/abs/2206.10449) [nucl-th].
- [35] H.-j. Xu, W. Zhao, H. Li, Y. Zhou, L.-W. Chen, and F. Wang, *Phys. Rev. C* **108**, L011902 (2023), [arXiv:2111.14812](https://arxiv.org/abs/2111.14812) [nucl-th].